Comparisons between the WRF data assimilation and the GNSS tomography technique in retrieving 3D wet refractivity field in Hong Kong

Zhaohui Xiong [1], Bao Zhang [1, *] and Yibin Yao [1]

[1] School of Geodesy and Geomatics, Wuhan University, Wuhan 430079;

* Correspondence: sggzb@whu.edu.cn; Tel.: +86-027-6875-8403

Abstract: Water vapor plays an important role in various scales of weather processes. However, there are limited means to accurately describe its 3-dimensional (3D) dynamical changes. The data assimilation technique and the Global Navigation Satellite System (GNSS) tomography technique are two of the limited means. Here, we conduct an interesting comparison between the GNSS tomography technique and the Weather Research and Forecasting Data Assimilation (WRFDA) (a representative of the data assimilation models) in retrieving Wet Refractivity (WR) in Hong Kong area during a wet period and a dry period. The GNSS tomography technique is used to retrieve WR from the GNSS slant wet delay. The WRFDA is used to assimilate the zenith troposphereic delay to improve the background data. The radiosonde data are used to validate the WR derived from the GNSS tomography, the WRFDA output, and the background data. The Root Mean Square (RMS) of the WR derived from the tomography results, the WRFDA output, and the background data are 6.50 mm/km, 4.31 mm/km, and 4.15 mm/km in the wet period. The RMS becomes 7.02 mm/km, 7.26 mm/km, and 6.35 mm/km in the dry period. The lower accuracy in the dry period is mainy due to the sharp variation of WR in the vertical direction. The results also show that assimilating GNSS ZTD into the WRFDA only slightly improves the accuracy of the WR and that the WRFDA WR is better than the tomographic WR in most cases. However, in a special experimental period when the water vapor is highly concentrated in the lower troposphere, the tomographic WR outperforms the WRFDA WR in the lower troposphere. When we assimilate the tomographic WR in the lower troposphere into the WRFDA, the retrieved WR is improved.

Keywords: GNSS Tomography; Wet Refractivity; Weather Research and Forecasting model; Data Assimilation

1 Introduction

Water vapor (WV), mostly contained in the troposphere, plays an important role in various scales of atmospheric processes. But due to its active nature, there are limited models and techniques that can accurately describe or monitor its 3-dimensional (3D) dynamical changes (Rocken et al., 1993).

The development of Global Navigation Satellite System (GNSS) technique and the densely deployed GNSS receivers provide us the opportunity to monitor the WV field in near real time. When GNSS signal travels through the neutral atmosphere, it undergoes time delay and bending due to atmospheric refractivity. This effect is usually called the tropospheric delay in the GNSS community (Altshuler, 2002). The tropospheric delay is usually considered as the product of the zenith delay and the mapping function (Lanyi, 1984; Niell, 1996). The Zenith Tropospheric Delay (ZTD) consists of two parts: the hydrostatic part and the wet part. The wet delay is mainly associated with the WV and reflects WV content in the troposphere. Bevis et al. (1992) introduced the principle of using GNSS Zenith Wet Delay (ZWD) to retrieve the Precipitable Water Vapor (PWV). Since then, many scientists carried out the GNSS PWV experiments (Askne and Nordius,1987; Bokoye et al., 2003; Yao et al., 2014; Lu et al., 2015; Shoji and Sato, 2016). Now, the GNSS PWV can be retrieved with an uncertainty of 1-2 mm in post-processing (Tregoning et al., 1998; Adams et al., 2011; Grejner-Brzezinska, 2013) or real-time modes (Yuan et al., 2014; Li et al., 2014; Li et al., 2015).

The GNSS WV tomography technique was first proposed to monitor the 3D or 4D WV in 2000 (Flores et al., 2000; Seko et al., 2000; Hirahara et al., 2000). Since then, many scientists have proposed refined methods to improve the GNSS WV tomography (Flores et al., 2001; Nilsson and Gradinarsky, 2006; Rohm and Bosy, 2011; Wang et al., 2014; Wang et al., 2014; Zhao and Yao, 2017). The tomographic inversion algorithm can be roughly categorized into two groups. One group solves the tomography equation in the least squares scheme or in the Kalman filter scheme with additional constraints or using a priori information (Flores et al., 2000; Rohm and Bosy, 2011; Cao et al., 2006; Zhang et al., 2017). The other group uses the algebraic reconstruction algorithm or similar methods (Bender et al., 2011; Wang et al., 2014; Zhao and Yao, 2017). Some scientists also use different methods from the above to solve the GNSS WR tomography problem (Nilsson and Gradinarsky, 2006; Perler et al., 2011; Altuntac, 2015). Besides the algorithm improvement, some scientists tried to optimize the voxel division (Chen and Liu, 2014) or use virtual reference stations (Adavi and Mashhadi-Hossainali, 2014) or use additional GNSS rays (Zhao and Yao, 2017) to increase the effective GNSS rays and thus improve the tomography results. Though the tomography technique has the advantages of (1) free of weather conditions and (2) retrieve 3D WR field in near real time, it still suffers some problems. The sparse distribution of the GNSS receivers and the bad satellite-receiver geometry lead to serious ill-posed and ill-conditioned problems, and also limit the WR retrieve resolution in both vertical and horizontal domains.

Besides the GNSS tomography technique, the WR can also be retrieved by data assimilation which is based on numerical weather prediction (NWP) models (Perler et al., 2011). The Weather Research and Forecasting (WRF) model is a state-of-the-art atmospheric modeling system that is used to simulate the dynamic processes of the atmosphere (Jankov et al., 2005; Carvalhoaabc et al., 2012). It is mainly developed and supported by Mesoscale and Microscale Meteorology (MMM) Laboratory of the National Center for Atmospheric Research (NCAR). And the WRF Data Assimilation (WRFDA) is designed to obtain the best estimate of the actual atmospheric state at any analysis time (Barker et al., 2004; Huang et al., 2008; Barker et al., 2012; Singh et al., 2017). Many studies have demonstrated that assimilating ZTD/PWV into WRFDA can improve the reanalysis water vapor field (Pacione et al., 2001; Faccani et al., 2005; Boniface et al., 2012; Bennitt and Jupp, 2012; Moeller et al., 2016; Lindskog et al., 2017). Besides the WRFDA model, the Japan Meteorological Agency (JMA) Mesoscale Numerical Weather Prediction Model (Nakamura et al., 2004) and AROME NWP system (Boniface et al., 2009) can also make use of ZTD\PWV data assimilation.

Though the GNSS tomography technique and the data assimilation technique belong to different fields, both of them could retrieve 3D WR field. It will be interesting to compare their capabilities in retrieving WR field under different weather conditions and to explore the feasibility to combine them. Such results may provides insights for the NWP community about this new technique and the possibility of assimilating the tomography results into the NWP models. For the GNSS community, they will get a better understanding of the WRF data assimilation and its capability in simulating the water vapor field. For this purpose, we conduct GNSS tomography and data assimilation experiments in Hong Kong area using SatRef Network in a wet period and a dry period. WR fields retrieved from GNSS tomography and WRFDA outputs are validated by the radiosonde data. We also explore the feasibility of assimilating the GNSS tomographic WR into the WRFDA to further improve the WR field.

2 Research Area and Data Analysis

The study area is within 113.75°E-114.5°E and 22°N-22.6°N as shown in Figure 1. There are 15 continues GNSS stations belonging to the Hong Kong SatRef Network deployed in the study area. They are all equipped with Leica GNSS receivers and antennas to receive the GNSS signals and automatic meteorological devices to record the temperature, pressure, and relative humidity. The average inter-distance between stations is about 10 km. The altitudes of the highest station (HKNP) and the lowest station (HKLM) are 354 m and 10 m. In GNSS tomography, we regard a network whose altitude differences of its stations are less than 1 km as a flat network. Therefore, the SatRef network is a flat network.

Two periods of GNSS observation data are processed to generate ZTD and Slant Wet Delay (SWD). One is a wet period from July 20 to 26, 2015 when Hong Kong suffered the heaviest daily rainfall of 2015 (191.3 mm rainfall on July 22). The other is a dry period from August 1 to 7, 2015 when Hong Kong is rainless. The details about the GNSS data processing and the SWD reconstruction can be found in Applendix A.
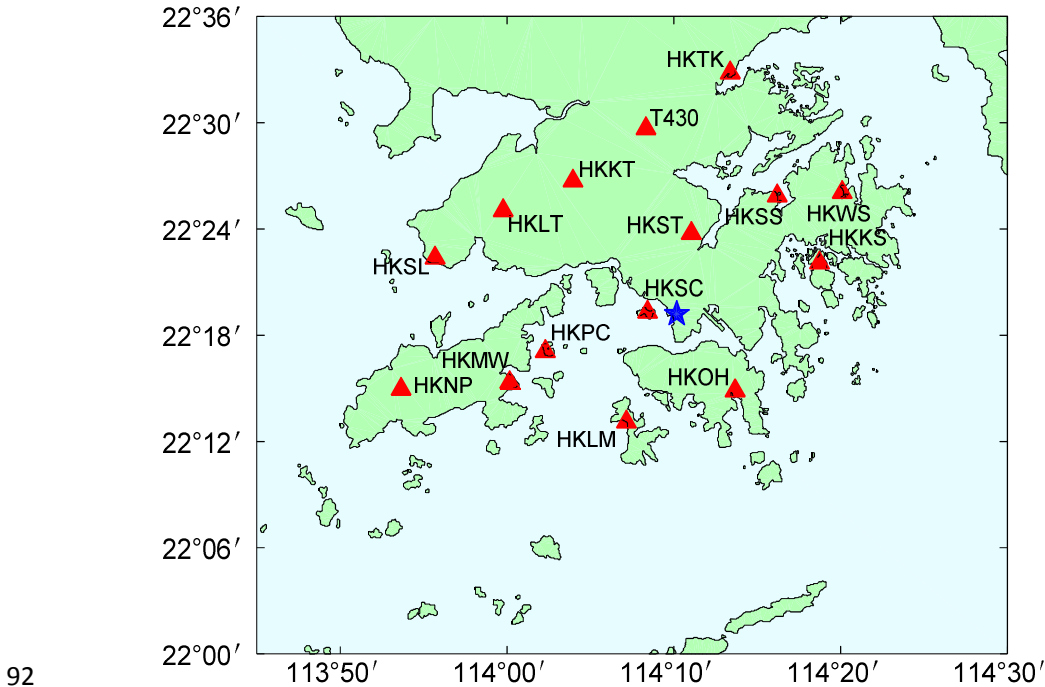

Figure 1. Research area of the experiment. The red triangles indicate the GNSS stations and the blue star indicates the radiosonde station in Hong Kong.

3 Method

3.1. WRF Data assimilation

The WRF model version 3.7 is used in this study. The WRFDA-3DVAR is used to assimilate the GNSS ZTD to improve the background data. The horizontal resolution of WRFDA output is set to 3 km. And the atmosphere is vertically divided into 45 layers. The pressure of the top layer is 50 hpa. There are 10 layers in the planetary boundary layer (PBL). We use the ZTD error output by the Bernese 5.0 software as obervation error. We use the reanalysis data from European Center for Medium-Range Weather Forecasts (ECMWF) ERA-Interim pressure levels and surface data as the background data, whose spatial resolution is $0.75° \times 0.75°$. And we run the WRFDA model at 0:00 UTC and 12:00 UTC, corresponding to the radiosonde observation time. The procedures to do the assimilation experiments are shown in Figure 2.
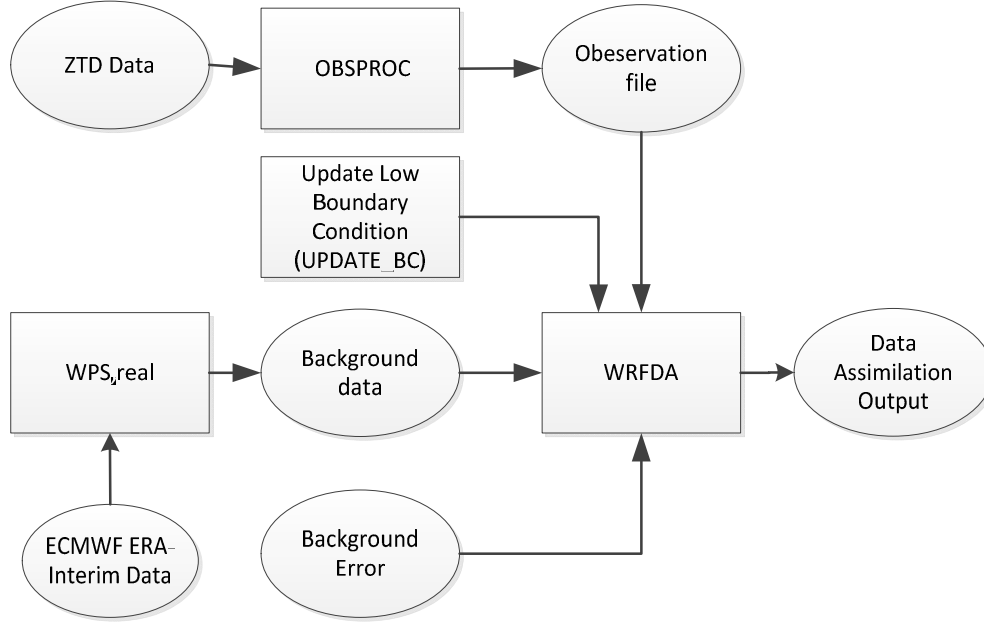
Figure 2. Flowchart of data assimilation using the WRF model.

107 The background data are processed by WRF preprocessing system (WPS). The WRFDA is run with the generic
108 CV3 option, and the default background error is adopted in this study. The GNSS ZTDs are the input
109 observations for WRFDA. We run WRFDA to obtain the data assimilation output, labeled as Output1. The
110 output from WPS and real.exe is labeled as Output2. We compare the WR derived from Output1 and Output2.
111 We use Equation (1) to calculate WR (Vedel and Huang, 2004) from the Output1 and Output2.

$$WR = \frac{P_w}{T} \times (k_1 + \frac{k_2}{T}) \tag{1}$$

112 where P_w is the water vapor pressure in each grid point in Pascal, T is the temperature in each grid point in

113 Kelvin. $k_1 = 2.21 \times 10^{-7}$ K/Pa, $k_2 = 3.73 \times 10^{-3}$ K²/Pa. We use Equation (2) to calculate P_w.

$$P_w = \frac{p \times q}{0.622} \tag{2}$$

114 where *p* is the pressure in Pascal, *q* is the specific humidity in g/g.

115 The WRFDA has many options for different physical parameterizations. In order to find the best choice for the
116 data assimilation experiment, we follow Chien et al. (2006) to set 12 schemes to do the sensitivity tests, which
117 are listed in Table 1. We carry out the sensitivity test at 00:00 UTC 22nd July in 2015. The domain size is set to
118 30×24 grids which just cover the study area. The grid size is 3 km × 3 km. We run WRFDA using the different
119 setting schemes. The radiosonde data are used to validate the wet refractivity derived by the WRFDA output.
120 Table 1 shows that all schemes have the same bias, standard deviation (STD), and Root Mean Square (RMS),
121 which suggests that the output wet refractivity is not affected by the physical parameterization settings in
122 WRFDA.

123 In this study, we use the Kain-Fritsch scheme (Kain and Frisch, 1990), WRF Single-Moment (WSM) 5-class
124 scheme (Hong et al., 2004) and Yonsei University PBL scheme (Hong et al., 2006), which are the same to Chien
125 et al. (2006). The other physical options include unified Noah land-surface model (Tewari et al., 2004), Revised

126 MM5 Monin-Obukhov scheme (Monin and Obukhov, 1954). The Rapid Radiative Transfer Model (Mlawer et
127 al., 1997) and Dudhia's scheme (Dudhia, 1989) are used for longwave radiation and shortwave radiation,
128 respectively.

129 **Table 1.** Physical parameterization schemes and statistics of bias, RMS, and STD of retrieved WR using
130 different schemes. Unit is mm/km.

	PBL physics	cumulus physics	microphysics	bias	STD	RMS
1	Yonsei University	Kain-Fritsch	WSM 5-class	-3.95	6.55	7.51
2	Yonsei University	Betts-Miller-Janjic	WSM 5-class	-3.95	6.55	7.51
3	Yonsei University	Grell-Freitas ensemble	WSM 5-class	-3.95	6.55	7.51
4	Yonsei University	Kain-Fritsch	Ferrier	-3.95	6.55	7.51
5	Yonsei University	Betts-Miller-Janjic	Ferrier	-3.95	6.55	7.51
6	Yonsei University	Grell-Freitas ensemble	Ferrier	-3.95	6.55	7.51
7	Mellor-Yamada-Janjic	Kain-Fritsch	WSM 5-class	-3.95	6.55	7.51
8	Mellor-Yamada-Janjic	Betts-Miller-Janjic	WSM 5-class	-3.95	6.55	7.51
9	Mellor-Yamada-Janjic	Grell-Freitas ensemble	WSM 5-class	-3.95	6.55	7.51
10	Mellor-Yamada-Janjic	Kain-Fritsch	Ferrier	-3.95	6.55	7.51
11	Mellor-Yamada-Janjic	Betts-Miller-Janjic	Ferrier	-3.95	6.55	7.51
12	Mellor-Yamada-Janjic	Grell-Freitas ensemble	Ferrier	-3.95	6.55	7.51

131 In order to figure out how sensitive the wet refractivity output is to the domain size, we carry out another
132 sensitive test at 00:00 UTC 22nd July in 2015. And we increase the domain size gradually from 30 × 24 grids to
133 190 × 184 grids. In each run, we validate the wet refractivity derived by the WRFDA output using the radiosonde
134 data. The statistical results of the sensitivity tests are shown in Figure 3. It shows that the smaller domain size
135 has the smaller bias, STD, and RMS. So, the domain size of the data assimilation experiment is set to 30 × 24
136 grids which just cover the study area.
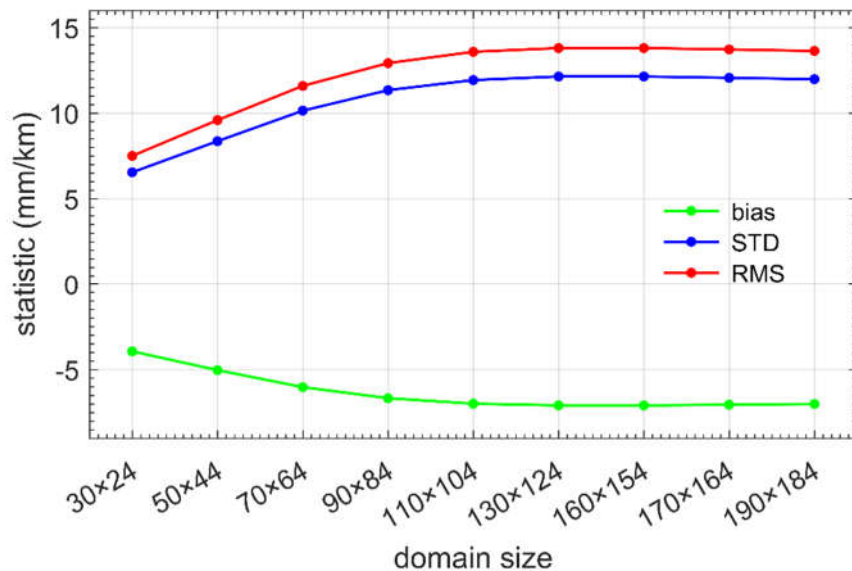
137

138 **Figure 3.** WR Statistics of sensitive test of domain size validated by radiosonde data.

139 *3.2. GNSS tomography*

140 The limited number of stations, flat vertical distribution of stations, and bad satellite-station geometry impose
141 serious ill-posed problem in the WR tomography. To well handle this problem, we use the tomography method
142 proposed by Zhang et al. (2017). This method is based on the adaptive Laplacian smoothing and Helmert

143   Variance Component Estimation. It also uses the meteorological data from each GNSS station to constrain the
144   WR near the ground. This tomography strategy is free of a priori information, which makes it an independent
145   technique and thus ensures the fairness when the tomography technique is compared with the WRFDA model.
146   The WR can be retrieved directly by this tomography strategy when the SWDs are used as observations. The
147   troposphere is vertically divided into 13 layers with a constant thickness of 800 meters, and horizontally divided
148   into grids whose resolution is ~10 km in longitudinal direction and ~8 km in latitudinal direction. The
149   tomography algorithm is described as follows:

150
$$\left.\begin{array}{l} \mathbf{Y} = \mathbf{AX} \\ \mathbf{0} = \mathbf{VX} \\ \mathbf{0} = \mathbf{HX} \\ \mathbf{0} = \mathbf{BX} \\ \mathbf{X}_m = \mathbf{X} \end{array}\right\} \tag{3}$$

151   where the first equation is the observation equation, $\mathbf{Y}$ is the vector of SWDs, $\mathbf{A}$ is the design matrix
152   consisting of intercepts in each voxel, $\mathbf{X}$ is the vector of WR in each voxel. The second to the forth
153   equations in Equation (3) are the vertical, horizontal, and boundary constraints. The fifth equation is used
154   to constrain the WR near the ground using the meteorological data at each GNSS station. $\mathbf{V}$, $\mathbf{H}$, and
155    $\mathbf{B}$ are design matrix for constraint equations. The boundary constraints are established by setting the
156   WR in the top layer to 0. The vertical and horizontal constraints are established by Laplacian smoothing
157   in the vertical and horizontal directions, respectively. The Laplacian smoothing can be described as:

158
$$x_1 + x_2 + x_3 + x_4 - qx_0 = 0 \tag{4}$$

159   where the WR x_0 equals the weighted average WR of its nearest four voxels in the same plane, q is
160   the smoothing factor.

161   In a least square scheme, the solution can be found by:

162
$$\mathbf{X} = (\mathbf{A}^T\mathbf{A} + \lambda_1\mathbf{V}^T\mathbf{V} + \lambda_2\mathbf{H}^T\mathbf{H} + \lambda_3\mathbf{B}^T\mathbf{B} + \lambda_4)^{-1}(\mathbf{A}^T\mathbf{Y} + \lambda_4\mathbf{X}_m) \tag{5}$$

163   Where λ_i (i = 1, 2, 3, 4) are the weights of corresponding constraints.

164   In Zhang et al. (2017), the solution is found in an iterative feedback-update process, which is be simply
165   described as follows:

166   (a) Establish the initial constraints and initialize their weights as 1, namely $\lambda_1 = \lambda_2 = 1$, λ_3 is set to a large
167   value, λ_4 is set to 1; λ_3 and λ_4 are not updated in the following run.

168   (b) Determine the values of λ_1 and λ_2 by Helmert Variance Component Estimation method and calculate
169   the tomography solutions by Equation (5);

170   (c) Update the smoothing factors by using the solutions in (b):

171
$$q = \begin{cases} n & \text{if} \quad x_0 < x_m \\ \dfrac{\sum\limits_{i=1}^{n} x_i}{x_0} & \text{if} \quad x_0 > x_m \end{cases} \qquad (6)$$

172　where n is the number of voxels used to calculate the weighted average. x_m is a threshold set to prevent

173　updating the smoothing factor by inaccurate solutions. The initial value for x_m is half of the maximum wet

174　refractivity in the solutions. x_m is updated by multiplying x_m by a scale factor, say 0.9, after each run until it

175　is no larger than 3 times the mean square error of $\mathbf{X}$.

176　(d) Use the new smoothing factors in (c) to update the horizontal and vertical constraints and redo (b) and (c)
177　until the mean square error of the solution differences between this run and the previous run approaches a stable
178　value. In practice, we set a threshold of 20 iterations which is enough to ensure a stable solution.

179　**4 Results**

180　The radiosonde data are used to validate the WR derived from GNSS tomography, the Output1 and the Output2.
181　Since the radiosonde launches at 0:00 and 12:00 UTC daily, the WR at these epochs are validated. Equation (1)
182　is also used to calculate WR from radiosonde data. The vertical coordinates of the Output1 and the Output2 are
183　converted to geopotential heights by NCAR Command Language (NCL) (UCAR/NCAR/CISL/VETS, 2013)
184　and the geodetic heights of tomographic results are converted to normal height. The slight differences between
185　geopotential heights and normal heights are neglected. We interpolate the Radiosonde to tomographic nodes
186　since the former has a much higher resolution ~23 layers from 0 to 10 km height than the latter (13 layers) and
187　thus we can get a higher interpolation accuracy. We use a bilinear interpolation method in the horizontal domain
188　and a linear interpolation method in the vertical direction. By these methods, we interpolate the WR derived
189　from the Output1, the Output2 and radiosonde data to the tomography nodes. Finally, the WR are validated by
190　the radiosonde data. For simplicity, WR from radiosonde data, and GNSS tomography are denoted as
191　"Radiosonde", and "Tomography" hereinafter.

192　Figures 4 and 5 show the vertical profiles of the Radiosonde, the Output1, the Output2 and the Tomography in

193　the July and August periods, respectively. The Output1, the Output2, and the Tomography agree well with the

194　Radiosonde, which indicates that these three methods successfully retrieved the vertical profile of the WR. It is

195　also observed that the Output1, the Output2, and the Tomography agree better with the Radiosonde in the July

196　period than in the August period. This difference should be due to the vertical distribution of WR. Though Hong

197　Kong suffered heavy rain in the July period, the WR was more evenly distributed from 0 to 10 km height than

198　that in the August period. In the dry August period, the WR was highly concentrated in the lower troposphere

199　(< 6 km) and its vertical changes were very sharp. This situation decreased the performance of the tomography

200　technique and the data assimilation technique. This also indicate that the tomography technique has decreased

201　capabilities in retrieving WR in highly changing troposphere. Compared with the Output2, the Output1 is

202　slightly improved by reducing the mean absolute error (MAE) by 1.25 mm/km. The difference between the

203　Tomography and the Output1 is obvious at some time epochs in the dry period (e.g., 12:00 on August 4 and 5).
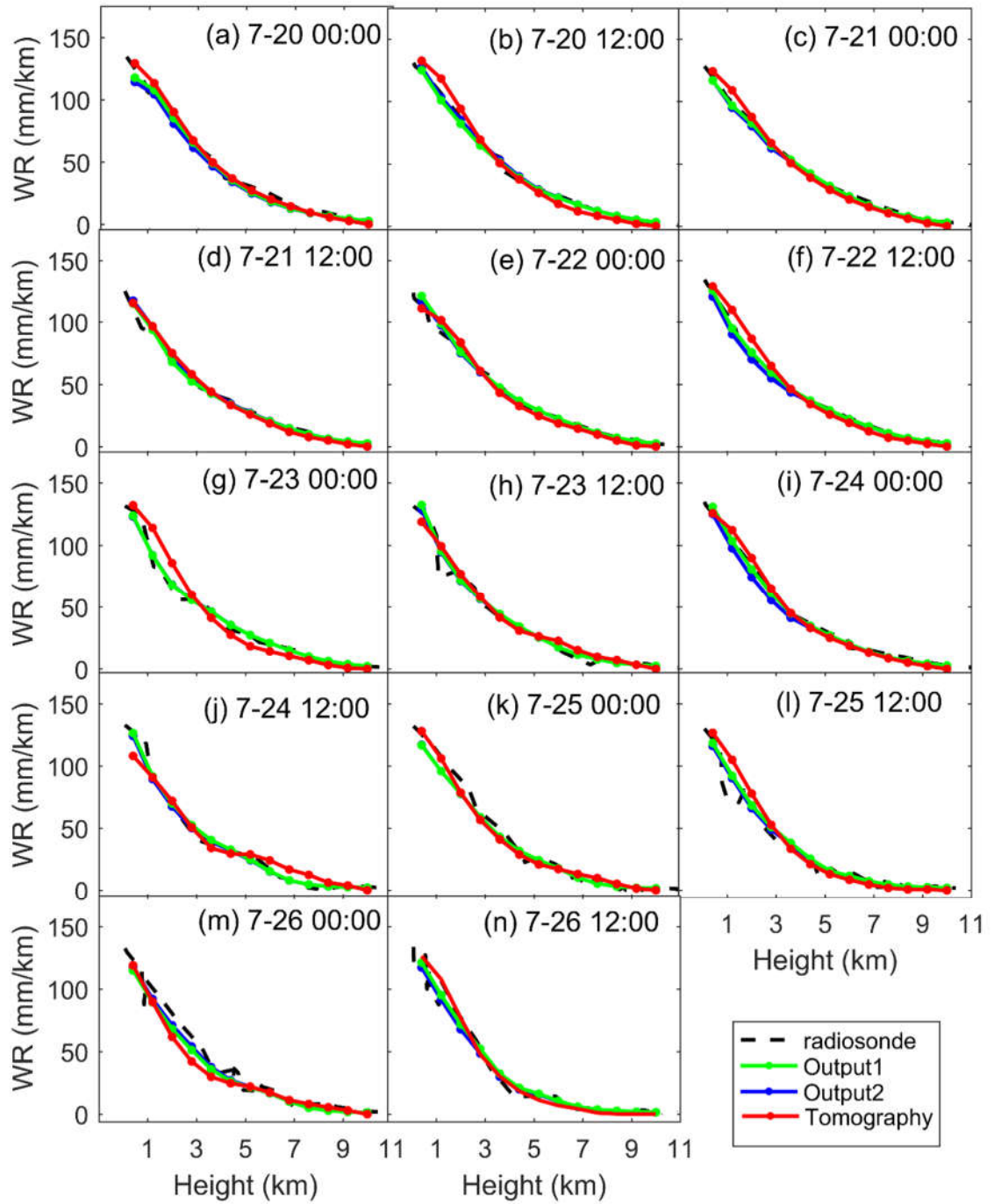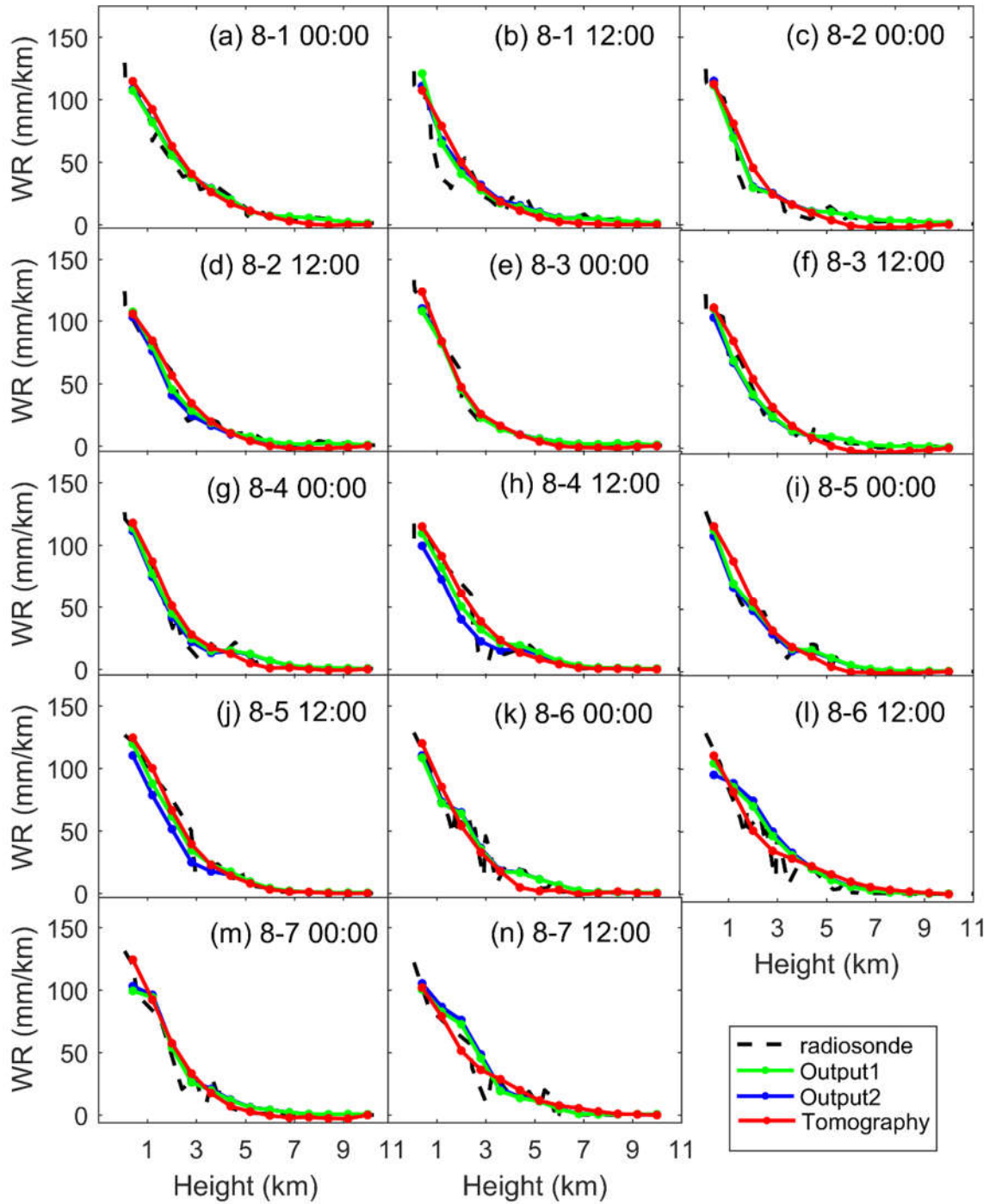
**Figure 4.** Comparisons among WR derived from Output1, Output2, Tomography, and Radiosonde in the wet period, 2015.

Figure 5. Comparisons among WR derived from Output1, Output2, Tomography, and Radiosonde in the dry period, 2015.

Figure 6 shows the statistics of the bias, STD, and RMS of the Tomography, the Output1, and the Output2 validated by the Radiosonde at different heights. In the wet period, bias of the Output1 is smaller than that of the Output2, but the differences are not obvious in terms of STD and RMS. In the dry period, the bias of the Output1 in the lower troposphere is slightly greater than that of the Output2. Overall, the differences between the Output1 and the Output2 are not significant.

In the wet period, the bias, STD, and RMS of the Tomography are greater than that of the Output1 in most of the time. But in the dry period, the STD and RMS of the Tomography tend to be smaller than that of the Output1 in the lower troposphere, but its bias is still greater. In general, the WRFDA performs better than the tomography

218 technique in most of the cases, but the RMS of Tomography validated by the Radiosonde in 400 m, 1600 m and
219 2400 m height is smaller than WRFDA output as shown in Figure 6f. So, in the lower troposphere in the dry
220 period the tomography performed better than the WRFDA in terms of RMS.
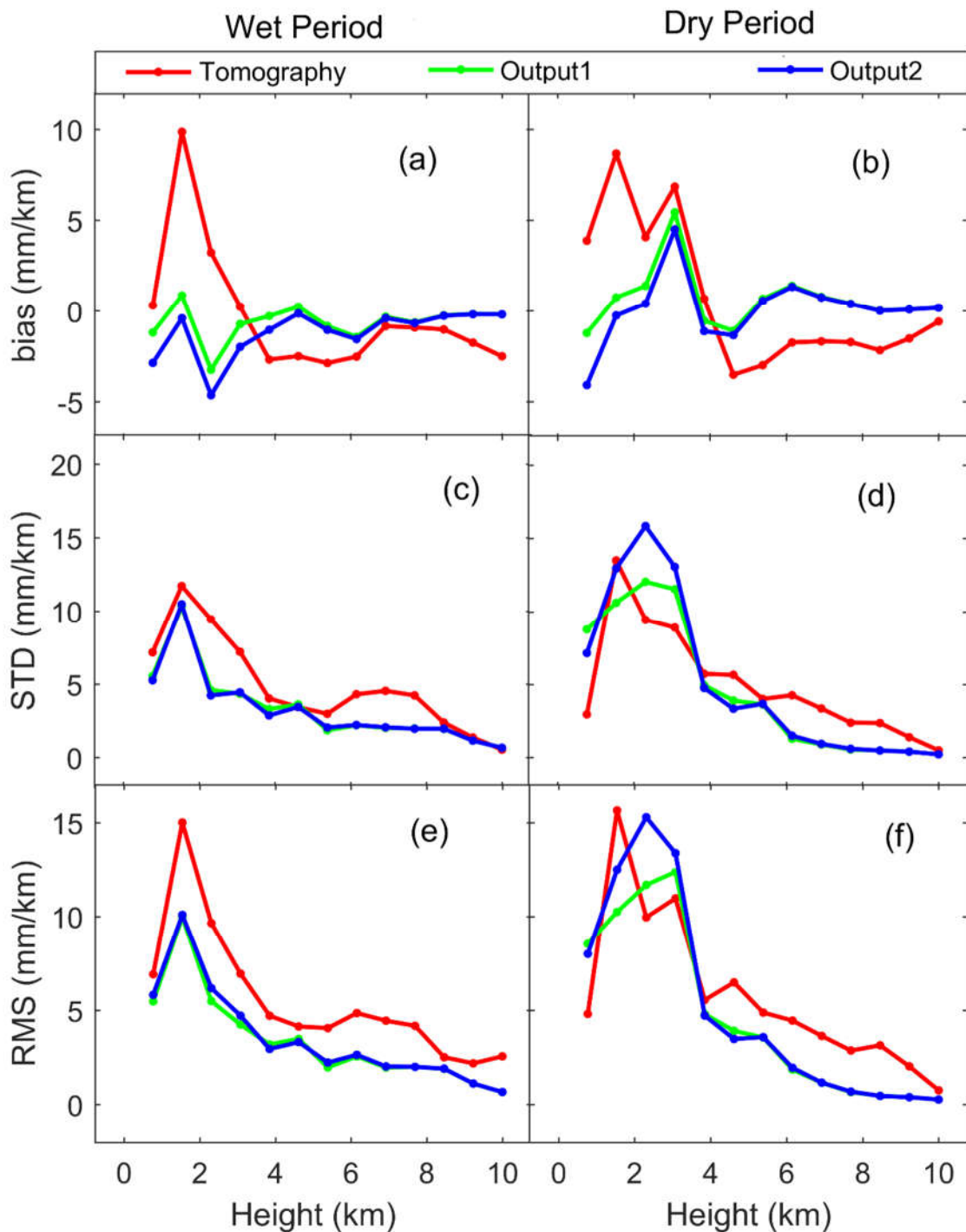
Figure 6. Statistics of bias, STD, and RMS of Tomography, Output1, and Output2 validated by the Radiosonde.

223 Table 2 shows the bias, STD, and RMS of the Tomography, the Output1, and the Output2 validated by the
224 Radiosonde. In the whole troposphere in the wet period, the Tomography has the smallest bias but the largest
225 STD and RMS. The Output1 and the Output2 have the similar STD and RMS that are much smaller than that
226 of the Tomography. But the Output2 has the largest bias than the Output1 and the Tomography. In the lower
227 troposphere in the wet period, the Output1 has the smallest STD and RMS while the Tomography has the largest

228 ones. The bias of Tomography is positive in the low troposphere but negative in the upper troposphere, this
229 should be due to the vertical smoothing constraints imposed on the WR. In the upper troposphere in the wet
230 period, Tomography has the largest bias, STD, and RMS while the Output1 has the smallest ones. Overall, both
231 the tomography and the WRFDA results have larger bias, STD, and RMS in the lower troposphere than in the
232 upper troposphere, indicating both the tomography technique and the data assimilation technique has deceased
233 capabilities in the lower troposphere.

234 In the whole troposphere in the dry period, the Output2 has the smallest bias but the largest STD and RMS. The
235 STD and RMS of the Tomography are larger than the Output1. In the lower troposphere in the dry period, the
236 Output2 has the largest RMS and STD while the Output1 as the smallest ones. In the low troposphere in the dry
237 period, the performance of the Tomography is not as good as the Output1 in terms of RMS. However, in the
238 upper troposphere in the dry period, the Tomography has relatively larger bias, STD and RMS than the WRFDA
239 results.

240 **Table 2.** Statistics of bias, RMS and STD of Tomography, Output1 and Output2 validated by the
241 radiosonde WR. Unit is mm/km.

		Wet Period			Dry Period		
		bias	STD	RMS	bias	STD	RMS
Total	Output1	-0.64	4.11	4.15	0.63	6.34	6.35
	Output2	-1.19	4.15	4.31	0.10	7.28	7.26
	Tomography	-0.31	6.51	6.50	0.63	7.01	7.02
Low (< 5.6 km)	Output1	-0.74	5.37	5.40	0.77	8.62	8.61
	Output2	-1.73	5.37	5.62	-0.19	9.90	9.85
	Tomography	0.80	8.20	8.19	2.52	8.83	9.13
Upper (≥ 5.6 km)	Output1	-0.51	1.75	1.81	0.47	0.86	0.97
	Output2	-0.55	1.77	1.84	0.45	0.91	1.01
	Tomography	-1.60	3.26	3.62	-1.57	2.63	3.05

242 In general, assimilating GNSS ZTD into the WRFDA has slightly improved the WR retrieval by decreasing the
243 RMS by 0.2 mm/km. The WR derived from the Output1 and the Output2 has apparently smaller RMS than the
244 tomographic WR (4.15 mm/km vs. 6.50 mm/km and 4.31 mm/km vs. 6.50 mm/km, respectively). The results
245 obtained from WRFDA and tomography are better in the wet period than in the dry period, which is mainly due
246 to the sharp vertical variation of WR in the dry period.

5 Discussion

248 In the dry period, due to the sharp vertical variations of WR, the Tomography, the Output1 have decreased
249 performance in retrieving the WR, especially in the lower troposphere. Compared with the results in the wet
250 period, the RMS of the Tomography and the Output1 increases by 0.94 mm/km, 3.24 mm/km in the dry period,
251 respectively. The accuracy decrease is more significant in the Output1 than in the Tomography, resulting in that
252 the tomographic WR becomes better than the Output1 (Figures 6d and 6f) in the low troposphere.

253 When assimilating ZTD into the WRFDA, we only use the total water vapor and cannot use the vertical profile
254 of water vapor. This leads to that the assimilation of ZTD has limited improvement in retrieving the vertical

255 structure of the WR. Therefore, it is natural to consider assimilating the tomographic WR into the WRFDA to
256 improve the retrieval of the vertical structure of WR. At present, WRFDA could not assimilate WR directly,
257 but can assimilate meteorological parameters such as relative humidity, temperature and pressure. To assimilate
258 the tomographic WR, we convert WR to relative humidity.

259 The relationship between relative humidity (RH) and P_w is shown as Equation (7).

$$RH = \frac{P_w}{P_s} \qquad (7)$$

260 where P_s is the saturated water vapor pressure which is related to temperature and can be calculated by Wexler

261 formula (Wexler, 1976,1977). The P_w is calculated by Equation (1). The needed temperature and pressure

262 data are from the Output2.

263 After converting the tomographic WR to RH, we assimilate the RH together with the corresponding temperature
264 and pressure into the WRFDA. Then, the similar procedures as described in Section 3.1 are performed to
265 generate new WRFDA output.

266 The Tomography agrees better with the Radiosonde than the Output1 and the Output2 in the lower troposphere
267 below 3 km at 12:00 on August 6 (Figure 5l) and at 12:00 on August 7 (Figure 5n). So, we assimilate the
268 tomographic WR below 3 km into the WRFDA at these two epochs. The generated output data are denoted as
269 "Output3". The difference between Output3 and Radiosonde is denoted as "DA-Tomo". The difference between
270 Output1 and Radiosonde is denoted as "DA-ZTD". The difference between Tomography and Radiosonde is
271 denoted as "Tomo". The MAE at different heights at 12:00 on August 6 and 7 are shown in Figure 7.

272
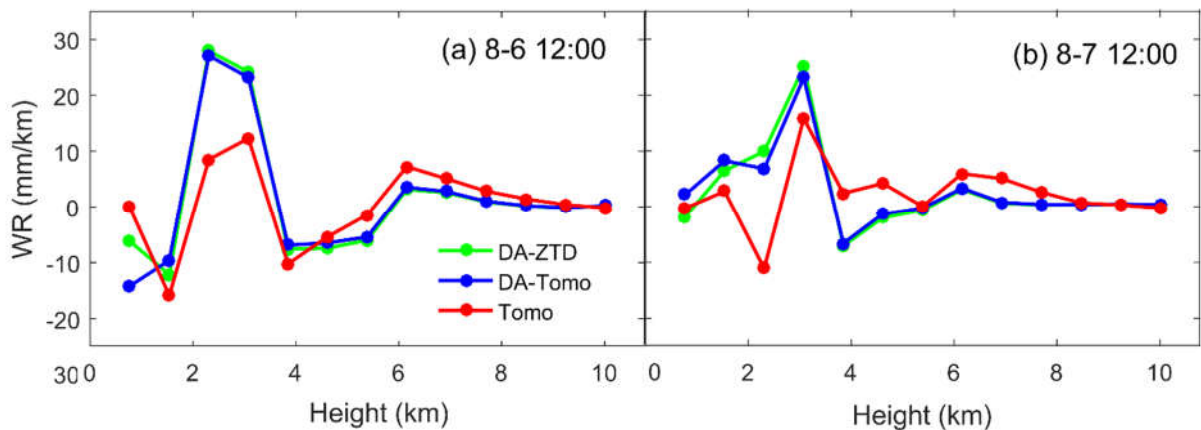
273

274 **Figure 7.** Differences between WR obtained by various methods and radiosonde WR.

275 Figure 7 shows that the DA-ZTD is very close to the DA-Tomo. The MAE of DA-ZTD is 6.04 mm/km and the
276 MAE of DA-Tomo is 5.92 mm/km. This indicates that assimilating tomographic WR into the WRFDA can
277 slightly improve the WR retrieve. But the large uncertainty (8.35 mm/km) of tomography WR in the lower
278 troposphere limit the improvement.

279 **6 Conclusions**

280 GNSS WR tomography and data assimilation experiments are conducted in Hong Kong during a wet and a dry
281 period to test the capabilities of the tomography technique and the WRFDA in retrieving WR. The results show

282 that both the tomography technique and the data assimilation technique can retrieve WR that agrees well with
283 the radiosonde data.

284 In the wet period in the whole troposphere, the RMS of Tomography, the Output1 and the Output2 are 6.50
285 mm/km, 4.31 mm/km, and 4.15 mm/km. The RMS becomes 7.02 mm/km, 6.35 mm/km, and 7.26 mm/km in
286 the dry period. Both methods obtained better WR in the wet period than in the dry period. We infer that the
287 sharp vertical variations of WR reduced the WR retrieving accuracy in the dry period. In most of the cases, the
288 Output1 outperforms the tomographic WR but the tomographic WR is better than the Output1 in the lower
289 troposphere in the dry period. By assimilating better tomographic WR in the lower troposphere into the WRFDA,
290 we slightly improve the retrieved WR.

291 The above results suggest that both the WRFDA and the tomography technique can retrieve good WR but also
292 have drawbacks. If we combine the two by assimilating good tomographic WR into the WRFDA, we may
293 further improve the performance of the WRFDA in retrieving the water vapor field.

294

295 *Data availability*. All the data used in this paper are available upon request by email (sggzb@whu.edu.cn).

296 **Appendix A**

297 The GNSS observation data are processed by the precise point positioning module in Bernese 5.0 software

298 using the same settings as detailed in Zhang et al. (2017). The International GNSS Service final orbit and clock

299 products are used. The differential code Biases (DCB) is corrected by products from the Center for Orbit

300 Determination in Europe. Antenna phase center offsets and variations, phase wind-up, Earth tides, Earth rotation,

301 ocean tides and relativistic effects are corrected by conventional methods detailed in (Kouba and Héroux, 2001).

302 We use the ionosphere-free combination of double frequencies to eliminate the first order ionospheric delay

303 and the higher-order terms are ignored. The tropospheric delay models are Saastamoinen model (Saastamoinen,

304 1972) and Niell mapping functions (Niell, 1996). The cut-off elevation angle is 10°. The station coordinates

305 and ZTDs are estimated simultaneously. Accurate zenith hydrostatic delays (ZHD) are estimated by using the

306 in-situ pressure observations and Saastamoinen model. The ZWD is estimated by removing the ZHDs from the

307 corresponding ZTDs. The SWD is reconstructed by mapping the ZWD and horizontal gradients onto the ray

308 direction. The phase residuals are added to SWD to consider the inhomogeneity of the troposphere.

309 *Conflicts of Interest*. The authors declare no conflict of interest.

316 **References**

317 Adams, K.; Fernandes, S.; Maia, F. GNSS Precipitable Water Vapor from an Amazonian Rain Forest Flux
318 Tower. Journal of Atmospheric & Oceanic Technology, 28(10):1192-1198, doi: 10.1175/jtech-d-11-00082.1,
319 2011.

320   Adavi, Z; Mashhadi-Hossainali, M. 4D tomographic reconstruction of the tropospheric wet refractivity using
321   the concept of virtual reference station, case study: northwest of Iran. M. Meteorol Atmos Phys, 126(3-4):
322   193-205. doi:10.1007/s00703-014-0342-4,2014.

323   Altshuler E E. Tropospheric range-error corrections for the Global Positioning System. IEEE Transactions on
324   Antennas & Propagation, 46(5):643-649, doi: 10.1109/8.668906, 2002.

325   Altuntac, E. Quasi-Newton Approach for an Atmospheric Tomography Problem. eprint arXiv:1511.08022,
326   Available at: https://arxiv.org/pdf/1511.08022.pdf   (accessed on 4 May 2018) , 2015.

327   Askne, J.; Nordius, H. Estimation of Tropospheric Delay for Microwaves from Surface Weather Data. Radio
328   Sci., 22(3): 379-386, doi: 10.1029/rs022i003p00379, 1987.

329   Barker, D.; Huang, Y.; Liu, Z.; Auligné, T.; Zhang, X.; Rugg, S.; Demirtas, M. The weather research and
330   forecasting model's community variational/ensemble data assimilation system: WRFDA. Bulletin of the
331   American Meteorological Society,93(6), 831-843, doi: 10.1175/BAMS-D-11-00167.1, 2012.

332   Barker, M.; Huang, W.; Guo, R.; Bourgeois, J.; Xiao, N. A three-dimensional variational data assimilation
333   system for MM5: Implementation and initial results. Monthly Weather Review, 132(4), 897-914, doi:
334   10.1175/1520-0493(2004)132<0897:ATVDAS>2.0.CO;2, 2004.

335   Bender, M.; Dick, G.; Ge, M.; Deng, Z.; Wickert, J.; Kahle, G.; Tetzlaff, G. Development of a GNSS water
336   vapour tomography system using algebraic reconstruction techniques. Advances in Space Research, 47(10):
337   1704-1720, doi: 10.1016/j.asr.2010.05.034, 2011.

338   Bennitt, V.; Jupp, A. Operational assimilation of GPS zenith total delay observations into the Met Office
339   numerical weather prediction models. Monthly Weather Review, 140(8), 2706-2719, doi:10.1175/MWR-D-
340   11-00156.1, 2012.

341   Bevis, M.; Businger, S.; Herring, A.; Rocken, C.; Anthes, A.; Ware, H. GPS meteorology: remote sensing of
342   atmospheric water vapor using the global positioning system. J. Geophys. Res., 97(D14): 15,787-15,801, doi:
343   10.1029/92JD01517, 1992.

344   Bokoye, I.; Royer, A.; O'Neill, T.; Cliche, P.; McArthur, B.; Teillet, M.; Thériault, M.. Multisensor analysis
345   of integrated atmospheric water vapor over Canada and Alaska. J. Geophys. Res., 108(D15): 4480, doi:
346   10.1029/2002jd002721, 2003.

347   Boniface, K.; Ducrocq, V.; Jaubert, G.; Yan, X.; Brousseau, P.; Masson, F.; Doerflinger, E. Impact of high-
348   resolution data assimilation of GPS zenith delay on Mediterranean heavy rainfall forecasting. Annales
349   Geophysicae, 27: 2739-2753, doi:10.5194/angeo-27-2739-2009, 2009.

350   Cao, Y.; Chen, Y.; Pingwha, I. Wet Refractivity Tomography with an improved Kalman-Filter Method.
351   Advances in Atmospheric Sciences, 23(5):693-699, doi: 10.5194/angeo-35-87-2017, 2006.

352   Carvalhoaabc, D. A sensitivity study of the WRF model in wind simulation for an area of high wind energy.
353   Environmental Modelling & Software, 33(7):23-34, doi:10.1016/j.envsoft.2012.01.019, 2012.

354   Chen, B.; Liu, Z. Voxel-optimized regional water vapor tomography and comparison with radiosonde and
355   numerical weather mode. J Geod, 88, 691–703,doi: 10.1007/s00190-014-0715-y, 2014.

356   Chien F C, Hong J S, Chang W J, et al. A sensitivity study of the WRF model. Part II: verification of
357   quantitative precipitation forecasts[J]. Atmos. Sci, 2006, 34(3): 261-276.

358   Dudhia, J. Numerical Study of Convection Observed during the Winter Monsoon Experiment Using a
359   Mesoscale Two-Dimensional Model. J.atmos., 46(46): 3077-3107, doi: 10.1175/1520-
360   0469(1989)046<3077:nsocod>2.0.co;2, 1989.

361   Faccani, C.; Ferretti, R.; Pacione, R.; Paolucci, T.; Vespe, F.; Cucurull, L. Impact of a high density GPS
362   network on the operational forecast. Advances in Geosciences, 2, 73-79, doi:10.5194/adgeo-2-73-2005, 2005.

363   Flores, A.; De Arellano, G.; Gradinarsky, P.; Rius, A. Tomography of the Lower Troposphere Using a Small
364   Dense Network of GPS Receivers. IEEE Transactions on Geoscience and Remote Sensing, 39(2): 439-447,
365   doi: 10.1109/36.905252, 2001.

366   Flores, A.; Ruffini, G.; Rius, A. 4D tropospheric tomography using GPS slant wet delays. Annales
367   Geophysicae, 18(2):223-234, doi: 10.1007/s005850050025, 2000.

368   Grejner-Brzezinska, A. GPS-PWV estimation and validation with radiosonde data and numerical weather
369   prediction model in Antarctica. Gps Solutions, 17(1):29-39, doi: 10.1007/s10291-012-0258-8, 2013.

370   Hirahara, K. Local GPS tropospheric tomography. Earth Planets & Space, 52(11):935-939, doi:
371   10.1186/bf03352308, 2000.

372   Hong, S.-Y., J. Dudhia, and S.-H. Chen, 2004: A Revised Approach to Ice Microphysical Pro-cesses for the
373   Bulk Parameterization of Clouds and Precipitation, Mon. Wea. Rev., 132,103–120.

374   Hong, Y.; Noh, Y.; Dudhia, J. A New Vertical Diffusion Package with an Explicit Treatment of Entrainment
375   Processes. Monthly Weather Review, 134(9):2318, doi: 10.1175/MWR3199.1, 2006.

376   Huang, Y.; Xiao, Q.; Barker, M.; Zhang, X.; Michalakes, J.; Huang, W.; Dudhia, J. Four-Dimensional
377   Variational Data Assimilation for WRF: Formulation and Preliminary Results. Monthly Weather Review,
378   137(1):299-314, doi:10.1175/2008MWR2577.1, 2008

379   Jankov, I.; Gallus Jr.; W. A.; Segal, M.; Shaw, B.; Koch, E. The Impact of Different WRF Model Physical
380   Parameterizations and Their Interactions on Warm Season MCS Rainfall. Weather & Forecasting,
381   20(6):1048-1060, doi:10.1175/WAF888.1, 2005.

382   Kain, J. S., and J. M. Fritsch, 1990: A one-dimensional entraining/ detraining plume model and its application
383   in convective parameterization, J. Atmos. Sci., 47, 2784–2802

384   Kouba, J.; Héroux, P., Precise point positioning using IGS orbit and clock products. GPS Solut. 5, 12-28,
385   doi:10.1007/PL00012883, 2001.

386   Lanyi, G. Tropospheric delay effects in radio interferometry. Telecommunications & Data Acquisition
387   Progress Report, 78,152-159. Available at: http://ipnpr.jpl.nasa.gov/progress_report/42-78/78N.PDF
388   (accessed on 4 May 2018), 1984.

389   Li, X.; Dick, G.; Ge, M.; Heise, S.; Wickert, J.; Bender, M. Real-time GPS sensing of atmospheric water
390   vapor: Precise point positioning with orbit, clock, and phase delay corrections. Geophysical Research Letters,
391   41(10): 3615-3621, doi: 10.1002/2014jd021486, 2014.

392   Li, X.; Zus, F.; Lu, C.; Dick, G.; Ning, T.; Ge, M.; Schuh, H. Retrieving of atmospheric parameters from
393   multi-GNSS in real time: validation with water vapor radiometer and numerical weather model. Journal of
394   Geophysical Research: Atmospheres, 120(14): 7189-7204, doi: 10.1002/2015jd023454, 2015.

395   Lindskog, M.; Ridal, M.; Thorsteinsson, S.; Tong, N. Data assimilation of GNSS Zenith Total Delays from a
396   Nordic processing centre. Atmospheric Chemistry & Physics, 17(22):1-22, doi: 10.5194/acp-2017-567, 2017.

397   Lu, C.; Li, X; Nilsson, T.; Ning, T.; Heinkelmann, R; Ge, M.; Schuh, H.. Real-time retrieval of precipitable
398   water vapor from GPS and BeiDou observations. Journal of Geodesy, 89(9), 843-856, doi: 10.1007/s00190-
399   015-0818-0, 2015.

400   Mlawer, J.; Taubman, J.; Brown, D.; Iacono, J.; Clough, A. Radiative transfer for inhomogeneous
401   atmospheres: RRTM, a validated correlated‐k model for the longwave. Journal of Geophysical Research
402   Atmospheres, 102(D14):16663-16682, doi: 10.1029/97JD00237, 1997.

403   Moeller, G.; Wittmann; C.; Yan, X.; Weber, R. GNSS tomography and assimilation test cases during the 2013
404   Central Europe floods. EGU General Assembly Conference, Vienna, Austria, 17-22 April 2016.

405   Monin, S.; Obukhov, M. Basic laws of turbulent mixing in the surface layer of the atmosphere. Contrib.
406   Geophys. Inst. Acad. Sci. USSR., 64:1963-1987. Available at:
407   https://www.mcnaughty.com/keith/papers/Monin_and_Obukhov_1954.pdf   (accessed on 4 May 2018), 1954.

408   Nakamura, H.; Koizumi, K.; Mannoji, N.; Data assimilation of GPS precipitable water vapor into the JMA
409   mesoscale numerical weather prediction model and its impact on rainfall forecasts. Journal of the
410   Meteorological Society of Japan. Ser. II, 82(1B): 441-452, doi: 10.2151/jmsj.2004.441,2004.

411   UCAR/NCAR/CISL/VETS; The NCAR Command Language (NCL, Version 6.1.2) [Software],
412   UCAR/NCAR/CISL/VETS, Boulder, Colo, 2013. Available at http://dx.doi.org/10.5065/D6WD3XH5.

413   Niell, E. Global mapping functions for the atmosphere delay at radio wavelengths. J. Geophys. Res., 101, doi:
414   3227-3246, 10.1029/95jb03048, 1996.

415   Nilsson, T.; Gradinarsky, L. Water vapor tomography using GPS phase observations: simulation results. IEEE
416   Transactions on Geoscience and Remote Sensing, 44(10): 2927-2941, doi: 10.1109/TGRS.2006.877755,
417   2006.

418   Pacione, R.; Sciarretta, C.; Faccani, C.; Ferretti, R.; Vespe, F. GPS PW assimilation into MM5 with the
419   nudging technique. Physics & Chemistry of the Earth Part A Solid Earth & Geodesy, 26(6-8):6-8,
420   doi:10.1016/S1464-1895(01)00088-6, 2001.

421   Perler, D.; Geiger, A.; Hurter, F. 4D GPS water vapor tomography: new parameterized approaches. Journal of
422   Geodesy, 85(8): 539-550, doi: 10.1007/s00190-011-0454-2, 2011.

423   Perler, D.; Geiger, A.; Rothacher, M. Determination of the 4D-Tropospheric Water Vapor Distribution by
424   GPS for the Assimilation into Numerical Weather Prediction Models. AGU Fall Meeting, San
425   Francisco ,USA, 5-9 December 2011.

426   Rocken, C.; Ware, R.; Van Hove, T.; Solheim, F.; Alber, C.; Johnson, J.; Solheim, F.; Alber, C.; Johnson, J.
427   Sensing atmospheric water vapor with the global positioning system. Geophys. Res. Lett., 20, 2631-2634, doi:
428   10.1029/93gl02935, 1993.

429   Rohm, W.; Bosy, J. The verification of GNSS tropospheric tomography model in a mountainous area.Adv.
430   Space Res., 47, 1721-1730, doi: 10.1016/j.asr.2010.04.017, 2011.

431   Saastamoinen, J. Atmospheric correction for the troposphere and stratosphere in radio ranging of satellites.
432   Use Artif. Satell. Geod., 15, 247-251, doi: 10.1029/GM015p0247, 1972.

433   Seko, H.; Shimada, S.; Nakamura, H.; Kato, T. Three-dimensional distribution of water vapor estimated from
434   tropospheric delay of GPS data in a mesoscale precipitation system of the Baiu front. Earth Planets & Space,
435   52(11):927-933, doi: 10.1186/bf03352307, 2000.

436   Shoji, Y.; Sato, K.; Yabuki, M.; Tsuda, T. PWV Retrieval over the ocean using shipborne GNSS receivers
437   with MADOCA real-time orbits. SOLA, 12: 265-271, doi: 10.2151/sola.2016-052, 2016.

438   Singh, S.; Mandal, M.; Bhaskaran, K. Impact of radiance data assimilation on the prediction performance of
439   cyclonic storm SIDR using WRF-3DVAR modelling system. Meteorology & Atmospheric Physics. (2):1-18,
440   doi:10.1007/s00703-017-0552-7, 2017.

441   Tewari, M.; Chen, F.; Wang, W.; Dudhia, J.; LeMone, A.; Mitchell, K.; Cuenca, H. Implementation and
442   verification of the unified noah land surface model in the WRF model. In Bulletin of the American
443   Meteorological Society., 2165-2170, doi:10.1007/s11269-013-0452-7, 2004.

444   Tregoning. P.; Boers, R.; O'Brien. D; Hendy, M. Accuracy of absolute precipitable water vapor estimates
445   from GPS observations. Journal of Geophysical Research: Atmospheres, 103(D22): 28701-28710, doi:
446   10.1029/98JD02516, 1998.

447   Vedel, H.; Huang, X. Impact of ground based GPS data on NWP forecasts. Journal of the Meteorological
448   Society of Japan, 82, 459-472, doi: 10.2151/jmsj.2004.459, 2004.

449   Wang, X.; Wang, X.; Dai, Z.; Ke, F.; Cao, Y.; Wang, F.; Song, L. Tropospheric wet refractivity tomography
450   based on the BeiDou satellite system. Advances in Atmospheric Sciences, 31(2), 355-362, doi:
451   10.1109/TGRS.2006.877755, 2014.

452   Wang, X., Dai, Z., Zhang, E., Fuyang, K. E., Cao, Y., Song, L.; Lianchun, S. Tropospheric wet refractivity
453   tomography using multiplicative algebraic reconstruction technique. Advances in Space Research, 53(1), 156-
454   162, doi: 10.1016/j.asr.2010.04.017, 2014.

455   Wexler, A. Vapor Pressure Formulation for Ice. Journal of Research of the National Institute of Standards-A.
456   Physics and Chemistry, 81A(1): 5-20, doi: 10.6028/jres.081A.003, 1977.

457   Wexler, A. Vapor Pressure Formulation for Water in Range 0 to f 00 °C. A Revision. Journal of Research of
458   the national Institute of Standards-A. Physics and Chemistry., 80A(5-6): 775-785, doi:
459   10.6028/jres.080A.071, 1976.

460   Yao, Y.; Zhang, B.; Xu, C.; Yan, F. Improved one/multi-parameter models that consider seasonal and
461   geographic variations for estimating weighted mean temperature in ground-based GPS meteorology. Journal
462   of Geodesy, 88(3):273-282, doi: 10.1007/s00190-013-0684-6, 2014.

463   Yuan, Y.; Zhang, K.; Rohm, W.; Choy, S.; Norman, R.; Wang, S. Real-time retrieval of precipitable water
464   vapor from GPS precise point positioning. Journal of Geophysical Research: Atmospheres, 119(16): 10044-
465   10057, doi: 10.1002/2014jd021486, 2014.

466   Zhang, B.; Fan, Q.; Yao, Y.; Li, X. An Improved Tomography Approach Based on Adaptive Smoothing and
467   Ground Meteorological Observations. Remote Sensing, 9(9):886, doi: 10.3390/rs9090886, 2017.

468   Zhao, Q.; Yao, Y. An improved troposphere tomographic approach considering the signals coming from the
469   side face of the tomographic area. Annales Geophysicae , 35(1): 87-95, doi: 10.5194/angeo-35-87-2017,
470   2017.

471